TiO 2 –SiO 2 Self-Standing Materials bearing Hierarchical Porosity: MUB-200(x) Series toward 3D-Efficient VOC Photoabatement Properties

Elodie Layan, Juhi Gupta, Isabelle Ly, Frédéric Nallet, Ahmed Bentaleb, Eric Laurichesse, Renaud Vallée, Jean-Luc Blin, Bénédicte Lebeau, Lebeau Bénédicte, et al.

TiO_2-SiO_2 Self-Standing Materials bearing Hierarchical Porosity: MUB-200(x) Series towards 3D-Efficient VOCs Photo-abatement Properties

Elodie Layan,[1] Juhi Gupta,[1] Isabelle Ly,[1] Frédéric Nallet,[1] Ahmed Bentaeb,[1] Eric Laurichesse,[1] Renaud Vallée,[1] Jean-Luc Blin,[2] Bénédicte Lebeau,[3] Frédéric Louërat,[1] Mickael Le Bechec,[4] Peter Moonen,[5,6] Thierry Toupance,[7] Thierry Pigot[4,*] and Rénal Backov[1,*]

[1] Université de Bordeaux, CRPP-UMR CNRS 5031, 115 Avenue Albert Schweitzer, 33600 Pessac, FRANCE. renal.backov@crpp.cnrs.fr

[2] Institut Jean Barriol, UMR CNRS 7053 L2CM, Université de Lorraine, Faculté des sciences et technologies, BP 70239, 54506 Vandoeuvre lès Nancy cedex, FRANCE

[3] CNRS - Institut de Science des Matériaux de Mulhouse (IS2M), 15, rue Jean Starcky - BP 2488-68057 Mulhouse cedex, France.

[4] Université de Pau et des Pays de l'Adour, E2S UPPA, CNRS, IMT Mines Ales, IPREM, 64000 Pau, France. thierry.pigot@univ-pau.fr

[5] Université de Pau et des Pays de l'Adour, E2S UPPA, CNRS, Total, LFCR, Pau, France

[6] Université de Pau et des Pays de l'Adour, E2S UPPA, CNRS, DMEX, Pau, France

[7] Université de Bordeaux, Institut des Sciences Moléculaires CNRS UMR 5255, Bât.A12, 351 cours de la libération, 33405 Talence cedex, France

Abstract

3D-photoactive self-standing porous materials have been synthesized through the integration of soft chemistry and colloids (emulsions, lyotrope mesophases and P25 titania nanoparticles). Final multiscale porous ceramics are bearing 700-1000 $m^2 g^{-1}$ of micro-mesoporosity depending on the P25 nanoparticle contents. The applied thermal treatment is not affecting the P25 anatase/rutile allotropic phase ratio. Photonic investigations correlated with the foams' morphologies suggest that the larger amount of TiO_2 is introduced, the larger is the walls' density, the smaller is the mean size of the void macroscopic diameters, both effects inducing a reduction of the photon transport mean free path (l_t) with the P25 content increases. A light penetration depth in the range of 6 mm is reached, depicting thus a real 3D-photonic scavenger behavior. The 3D-photocatalytic properties of the MUB-200(x) series, studied in a dynamic

"flow through" configuration show that, the highest photo-activity (concentration of acetone ablated and concentration of CO_2 formed) is obtained with the highest monolith height (volume), while providing an average of 75 % mineralization. These experimental results validate the fact that these materials, bearing a 3D-photo-activity, are paving the path for air purification operating with self-standing porous monolith-type materials, which are much easier to handle than powders. As such, the photocatalytic systems can be now advantageously miniaturized, offering thereby indoor air-treatment within vehicles/homes while limiting drastically the associated encumbrance. Beyond, this "volumic" counter-intuitive acting mode for light-induced reactions may find other relevant advanced applications towards photo-induced water splitting, solar fuel, dye sensitized solar cells (DSSC) while both optimizing photons scavenging and opening the path for miniaturization of the processes where encumbrance or foot-print penalty would be advantageously circumvented.

Keywords: Porous materials – Interfaces – VOC Abatement – Photonics- Integrative Chemistry

INTRODUCTION

Volatile organic compounds (VOCs) are major anthropogenic indoor air pollutants inducing severe health drawbacks.[1] As such, VOCs are not only intrinsic hazardous compounds, but can promote undesirable mechanisms with harmful by-products, including organic compounds, ozone, and secondary organic aerosols.[2] To circumvent these health issues, numerous air remediation techniques have been proposed while addressing VOCs removal.[3,4] Among the active techniques, photocatalyst oxidation is appearing as a promising VOCs removal method[5,6] where VOCs abatement is photoinduced ,at ambient temperature.[7,8] Common photocatalysts (semiconductor materials) used in photo-oxidation are TiO_2, ZnO, WO_3, ZnS, CdS and so forth.[9,10] As for now, titania (TiO_2) is certainly the most common oxide employed for photodegradation of organic pollutants[11–13] as well as battery electrodes and solar cells[14–17]

due to its unique band gap characteristics, environmental friendliness, high stability and low cost.[18–20] Despite, some drawbacks have to be circumvented, including the large band gap and high charge carrier recombination rate, which restrict its application under natural solar light irradiation. Significant efforts have been made to overcome the aforementioned disadvantages *via* various strategies such as metal or non-metal doping, co-doping, and coupling with other semiconductors that seem effective both for increasing the lifetime of the photo-excited pairs of charge carriers and shifting the band gap absorption limits to the visible range of irradiation light.[21,22] ConsideringTiO_2, UV light (about 3 % of solar radiation) is a common energy source for effective photo-oxidation properties[23] where the minimum band gap energy necessary for a photon to generate charge carriers over the titania anatase phase is 3.2 eV (388 nm wavelength photon absorption). Therefore, TiO_2 photoactivation occurs in wavelength below 388 nm, near the UV region.[9,24] Recently, some researchers have modified TiO_2 to enhance its photoactivity under visible light irradiation,[24–28] while several studies reported that titania crystalline character allows tuning intrinsically its photocatalytic efficiency.[29–35] Overall scenario where P25 Degussa TiO_2, composed of 75 % anatase and 25 % rutile, is appearing as the "photocatalytic" candidate of choice.[36] Aside and foremost, we do not have to forget that photoinduced-heterogeneous-catalytic processes are dealing with light-solid matter interaction. The highest challenge of optimizing solar irradiation is certainly to circumvent the drawback of the two-dimensional character of the active layer. Whatever the ingenious chemistry deployed at the molecular level,[21–26,29–39] common sense is pleading to increase the volume/surface ratio effectiveness of the photoactive materials in use, allowing both miniaturization of processes or/and minimizing foot print penalty. Recent studies have shown that light trapping within an active layer is a critical criterion for improving the efficiency of optoelectronic devices such as thin solar cells, photoelectrochemical cells and photo-fuel cells.[40–45] All these photonic investigations and photoconversion improvements are almost all dealing with

thin films or powders which still exhibit a surface behaviour rather than a real bulky one, overall configuration where our group has recently proposed 3D-photo-efficiency towards solar fuel production.[46]

It is in this vein of 3D-light-induced-catalysis that this research falls while dealing with 3D-VOCs photo-abatement within novel TiO_2@SiO_2 self-standing ceramics bearing hierarchical porosity**.** In this regard we definitely postulate here the new counter-intuitive paradigm of "thicker is better" when dealing with light scavenging foams dedicated toward photo-induced catalysis.

EXPERIMENTAL SECTION

Material syntheses. High purity dodecane (≥ 99 %), hydrochloric acid 37 wt% (HCl), tetraethylorthosilicate (≥ 99 %, TEOS), P25 Degussa titania nanoparticles were purchased from Sigma-Aldrich. Tetradecyltrimethylammonium bromide (TTAB) was supplied by Alfa Aesar, while dichloromethane (CH_2Cl_2, ACS-reagent RPE) was purchased from Carlo Erba. All the chemicals were used as received without any further purification. Deionized water was obtained using a Milli-Q water purification system.

Typically either 0.3, 0.8 or 1.2 g of P25 Degussa TiO_2 nanoparticles were dispersed in 16 g of a TTAB (35 wt%) water solution through a magnetic stirring of 1 h followed by a 10 mins sonication bath. We noticed that the TiO2 nanoparticles dispersion occurs quite easily, resulting in a monophasic milky-like dispersion. Then 5 g of HCl (37 wt%) were added prior adding 5 g of TEOS (pH 0.05). The solution was let under stirring 10 mins both to promote TEOS full hydrolysis and allow partial evaporation of the native ethanol. Then, 37 g of dodecane were emulsified drop-by-drop into a mortar through a manual stirring. The native direct oil-in-water emulsion was then transferred into several polypropylene tubes employed as canisters, where the sol-gel process is let to proceed during one week at 25 °C. Then the solidified emulsions were pulled out the canister and let to wash 12 h in dichloromethane

CH_2Cl_2. The wet materials were let to dry slowly in a desiccator for one week and let to dry further in air during three days. Finally a thermal treatment was applied to the materials to simultaneously sinter the silica network and calcine the TTAB surfactant employed as a mesoscopic templates. The thermal treatment was applied under atmospheric conditions as follow: a first temperature increase was applied at 2 °C min^{-1} until 180 °C with a 6 h plateau followed by a second temperature ramp at 1 °C min^{-1} to reach 700 °C with a 6 h plateau. The cooling process was uncontrolled and directed by the oven inertia. Final micro/meso-macroporous self-standing monoliths are labelled hereafter MUB-200(1), MUB-200(2) and MUB-200(3) while increasing the amount of titania nanoparticles introduced during the syntheses, where the acronym "M.U.B." stands for "Materials of the University of Bordeaux". Final self-standing catalysts are reported on Figure 1.

Photonic experiments.

The transport mean free path "l_t" and the absorption length "l_a" are determined on the whole visible spectrum from measurements of the total integrated forwards scattering owing to a white light illumination lamp (fiber coupled white light HL-2000-HP-FHSA, Ocean Optics) combined with an integrating sphere (fiber coupled integrating sphere FOIS-1, Ocean Optics) and a spectrometer (fiber spectrometer USB2000+VIS-NIR, Ocean Optics). The broadband signal of the light beam is focused on a 1 mm diameter spot prior to propagate through the sample and being collected on the 10 mm diameter circular aperture of the integrating sphere. These measurements, corrected with respect to the background signal, are then fitted with the transmission versus length of the samples T(L), as governed by the standard diffusion model,[47] in order to extract the transport mean free path and absorption length.

Photocatalytic experiments

Samples' photocatalytic efficiencies were evaluated with a dedicated one pass set-up (Figure S1 (a)). This reactor was composed of several inox parts (Pfeifer vacuum, Annecy France)

connected with ring seals and was heated to 35 °C with a heating cable to prevent any adsorption of VOCs. The samples were placed on an inox grid in the center of the reactor with an air inlet in the bottom and the outlet on the top to allow gas flow through the material. The reactor inlet was connected on one hand to a gas dilution bench (Serv'Instrumentation, Irigny France) mixing 120 cm^3 min^{-1} of synthetic air (80 % N_2 and 20 % O_2, Air Liquide France, 5.0 quality) with relative humidity (RH) fixed to 60 % and to another hand to a diffusion cell giving 60 cm^3 min^{-1} of acetone (around 420 ppmV) in dry air (Figure S1 (b)). The mixed gas flow was thus about 180 cm^3 min^{-1} of air with 40 % RH and 140 ppmV acetone. The reactor outlet was connected to a GC-methanizer-FID (ThermoFisher Trace 1300), with 2 GC lines, to continuously measure the concentration of acetone and CO_2 in the air flow. The first GC line, dedicated to VOC analysis, contained a 500 µL injection loop connected to a SSL Injector (250 °C split ratio 1), a column (Restek Rtx®1, 60 m, 0.53 mm, 3 µm, with a column flow 8 mL min^{-1} and an oven program 40 °C hold 5 mins, 180 °C rate 20 °C min^{-1} hold 2 mins) and a FID detector (250 °C, 350 mL min^{-1} Air, 40 mL min^{-1} Makeup gas (helium) and 35 mL min^{-1} H_2). The second GC line, dedicated the CO_2 quantification, contained a 2 500 µL injection loop connected to two columns (HS-N-60-80, 1m 1/8" sulfinert and HS-Q-60-80, 2M 1/8" sulfinert) with a backflush program. The CO_2 was converted to methane with a Nickel catalyzer (350 °C, 80 kPa H_2) and quantified with a second FID (250 °C, 350 mL min^{-1} of air, 20 mL min^{-1} of makeup gas and 15 mL min^{-1} of H_2). Acetone and CO_2 peak area conversions to concentration (ppmV) were evaluated from standard calibrations (data not shown). A third port of the reactor (on the upper side) was connected to a vacuum pump (Edwards Vacuum, Burgess Hill UK) and to dry N_2 for the samples conditioning step (3 cycles of vacuum 6.10^{-2} Torr and N_2 P atm), before every experiment. The irradiations were conducted with a lab-made UVA source containing 3 high power LEDs (Roithner LaserTechnik GmbH, Vienna Austria) giving 2.7 mW cm^{-2} at 365 nm at the sample position. The LEDs were posi-

tioned 3 cm from the material. Every experiment started with a conditioning step (3 cycles vacuum / N_2). Then the reactor was connected to the gas flux of acetone (180 mL min^{-1} of air with 40 % RH and 140 ppmV acetone). The material is first saturated with acetone in the dark and then when the concentration at the outlet of the reactor is equal to that at the inlet, the lamps are switched on.

Material Characterizations.

Scanning Electron Microscopy (SEM). The sample was properly broken and stuck onto an aluminum holder bearing silver paint. Then the fractured surface was metalized with gold/palladium sputtering. SEM images were acquired with a Hitachi TM-1000 tabletop scanning electron microscope operating with a 15 kV accelerating voltage. The Energy-Dispersive X-ray Spectroscopy (EDS) spectra and the mappings were obtained on a ZEISS EVO 50 scanning electron microscope equipped with an EDX EDAX detector. The electronic source was a lanthanum hexaboride tip (LaB_6) and the accelerating voltage was 20 kV.

Wide-Angle X-ray Scattering (WAXS). X-ray measurements were done on a Rigaku Nanoviewer (XRF microsource generator, MicroMax 007HF), with a copper rotating anode coupled to a confocal Max-Flux® Osmic mirror (Applied Rigaku Technolgies, Austin, USA) producing beam with a wavelength of 1.5418 Å or an energy of 8 keV. A wide-angle X-ray scattering with transmission geometry setting was chosen. Samples were put in a 1.5 mm diameter glass capillary (Glaskapillaren GLAS, Glas-Technik & Konstruktion, and Schönwalde-Glien, Germany) with a sample-detector distance of 125 mm providing access to angles in the 3–53° range. Images were collected on a MAR345 image plate detector (MARResearch, Norderstedt, Germany) and spectra were integrated with the FIT2D software (ERSF; http://www.esrf.eu/).

Small-Angle X-ray Scattering (SAXS). X-ray diffraction experiments were done on a XEUSS 2.0 device (XENOCS, Grenoble, FRANCE) with a GeniX3D system (XENOCS.

Micro-focus copper anode source coupled to a FOX3D single reflection mirror) delivering a monochromatic 8 keV beam (Cu Kα radiation, wavelength λ = 1.5418 Å). The beam is further collimated by a set of 2 motorized, scatter-less (4-blade) slits. The powdered samples were put into thin glass capillaries (optical path *ca.* 1.5 mm), and exposed for 2 h. Data is collected by a two-dimensional DECTRIS PILATUS-300k detector (Baden-Dättwill, SWITZERLAND) placed at a sample-to-detector distance of 1634 mm (calibrated with a silver behenate standard), giving access to a range of scattering wave vectors q between 0.007 $Å^{-1}$ and 0.23 $Å^{-1}$. Note that the XEUSS 2.0 device offers a wholly evacuated flight path, from the downstream end of the mirror to a few centimeters before the detector, including the samples. The 1D diffractograms (intensity *I* vs *q*) are obtained by processing the detector images with the FOXTROT software (collaboration between XENOCS and the SOLEIL synchrotron SWING beamline team (Gif-sur-Yvette, FRANCE).

Transmission Electron Microscopy (TEM) and High Resolution (HR-TEM). The samples were ground in a mortar then dispersed in ethanol. A drop of the dispersion was placed and dried on a TEM copper grid covered with a carbon film. The TEM pictures were obtained with a transmission electron microscope Hitachi H7650 operating at 80 kV. High Resolution TEM pictures were obtained with a Field Emission Gun (FEG) transmission electron microscope JEOL 2200FS operating at 200kV. A drop of the dispersion was placed and dried on a TEM copper grid covered either with a carbon film or a holey carbon film.

Gas sorption measurements. A Micromeritics 3Flex surface characterization analyzer (Micromeritics Instrument Corp, Norcross, GA) was used for all measurements. Prior to measurement, the samples were activated under secondary vacuum at 110 °C for 12 h. Activation at 350 °C for 12 h was also performed for comparison and led to similar results, indicating that the outgassing procedure was efficient for both temperatures. Nitrogen (N_2) adsorption isotherms measured at 77 K were collected and interpreted using multi-point Brunauer-

Emmett-Teller (BET) analysis for surface area determination over the range 0.05–0.30 relative pressure (P/P_0) and with a N_2 cross-sectional area of 0.162 nm^2. The mesoporous surface area has been determined using the Barrett, Joyner and Halenda (BJH) method while the microporous surface area has been estimated by difference between the BJH mesoporous surface area and the BET surface area, assuming that the macroporous surface area is negligible.

Mercury porosimetry. Intrusion/extrusion mercury measurements were performed using a Micromeritics Autopore IV apparatus to determine the scaffolds' macrocellular cell characteristics.

Helium pycnometry. Materials skeleton densities have been determined through helium pycnometer using a Micromeritics AccuPy 1330 apparatus. The samples were degassed under vacuum at 130 °C for 12 h prior performing the measurement.

Elemental analyses. Elemental analyses have been performed through ICP while using both ICP AES iCAP 6500 DUO and ICP AES iCAP 7400 Radia apparatus.

Thermogravimetric Analysis (TGA). TGA were performed in air using a TGA 5500 Discovery TA apparatus. The heating rate was set to 5 °C min^{-1}.

3D X-ray microtomography. Each sample was fixed on a carbon rod by means of double sided tape and the carbon rod was subsequently placed inside a Zeiss Xradia Versa 510 X-ray microscope by means of a pin vies to determine the three-dimensional morphological structure of the sample. The samples were scanned with a tube voltage of 40 kV. No beam filtration was applied. For each sample, 1601 projections with an exposure time of 12 s were acquired over an angular range of 360 °. The reconstructed voxel size was around 800 nm.

RESULTS AND DISCUSSION

Solid foams bearing a hierarchically organized porosity are, at first glance, unrealistic candidates to achieve efficient VOCs photoconversion. These porous materials are obtained by the synergistic template effects of lyotrope mesophases (concentrated micelles) which create the mesoporosity (pore diameters ranging from 2 nm to 50 nm) and concentrated oil-in-water bi-liquid foams promoting the open macroporosity (pore diameters above 50 nm), combined with the hydrolytic sol-gel chemistry that condenses the continuous hydrophilic phase.[48] As the inorganic skeleton is amorphous silica, the microporosity (pore diameters below 2 nm) relies on the statistical repartition of SiO_4 tetrahedra within the geometric space. These self-standing foams were labelled Si(HIPE),[48] H.I.P.E. stands as the acronym for High Internal Phase Emulsion.[48,49] They can be further hybridized to specify the catalytic applications.[50,51] When being purely inorganic, these foams have been recently employed as light scavengers in the field of random lasing,[52,53] where TiO_2 has been generated during the sol-gel process while employing titanium isopropoxide as molecular precursor to increase the inorganic skeleton refractive index, thereby optimizing the photon mean-free-path within the foams.[54] More recently we have employed Si(HIPE) as chemical reactor in which we have infiltrated during a second step, through vacuum, an acidic titania sol precursor where the TiO_2 nanoparticles were heterogeneously nucleated and grown at the Si(HIPE) internal wall surfaces (Plateau borders).[46] The synthesis proposed here is both simpler and one pot, where P25 Degussa titania nanoparticles are simply dispersed into the hydrophilic phase bearing hydrolysed TEOS and the TTAB lyotrope mesophase of the starting direct emulsions. In this approach P25 Degussa nanoparticles are employed both as catalytic sites and Mie scattering dots while silica is employed as inorganic glue allowing monolith-type self-standing-materials generation.

Materials characterization at the macroscopic length scale

The monolithic nature of the materials can be appreciated from Fig. 1 (a). Visualisations by means of X-ray tomography and SEM allow seeing the macroscopic cells induced by

the oil droplets templating effect (Fig. 1 (b-j)). First, we can say the macroscopic voids of the MUB-200(x) series resemble typical hollow spheres aggregation characteristic of Si(HIPE).[48] When regarding in details the macroscopic voids depicted in Fig. 1 (e-j) we can notice that the typical hollow spheres morphology is less and less pronounced while increasing the P25 nanoparticle contents, from the MUB-200(1) (Fig. 1 (b,e)) to the MUB-200(3) (Fig. 1 (i,j)), feature associated with a slight decrease of the macroscopic cell diameters. Indeed, while increasing the TiO_2 nanoparticle contents, the viscosity of the emulsion is increasing too, thereby the shear addressed to the oil droplets during the emulsification process is increasing, minimizing thereby their sizes. Aside, we can notice a small decrease of the throats connecting adjacent macroscopic cells. Here we may express the fact that some P25 TiO_2 nanoparticles are favouring the oil-water interfaces emulsions stability (pseudo Pickering-like effects),[55,56] thus limiting the coalescence phenomenon[57,58] and the associated films opening responsible of the throats generation.

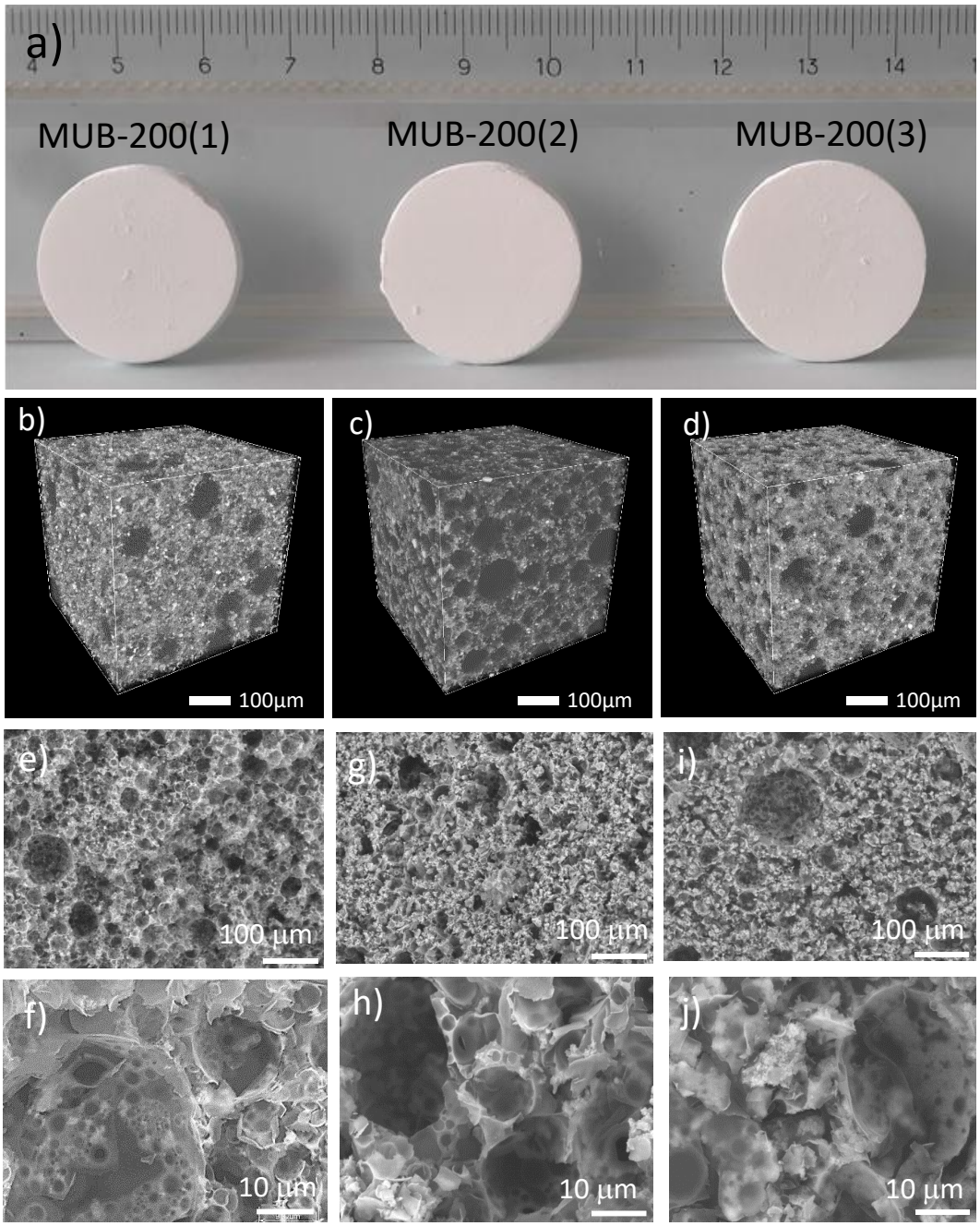

Figure 1. Macroscopic aspect of the MUB-200 series. (a) self-standing monoliths while increasing the TiO_2 contents from the right to the left leading respectively to the MUB-200(1), MUB-200(2) and MUB-200(3) materials, (b-d) X-ray images of the 3D microstructure of a 480µm^3 region of interest of the MUB-200(1-3), e-i) SEM investigations; (e-f) SEM of the MUB-200(1), (g-h) SEM of the MUB-200(2) and (i-j) SEM of the MUB-200(3). The big voids bearing diameters at the 100 µm length scale are not induced by the oil droplets templating effect but rather by the induction of some air bubbles during the emulsification process.

X-ray imaging and mercury porosimetry both enable obtaining a pore size distribution, expressing on a more quantitative approach (Figure 2).

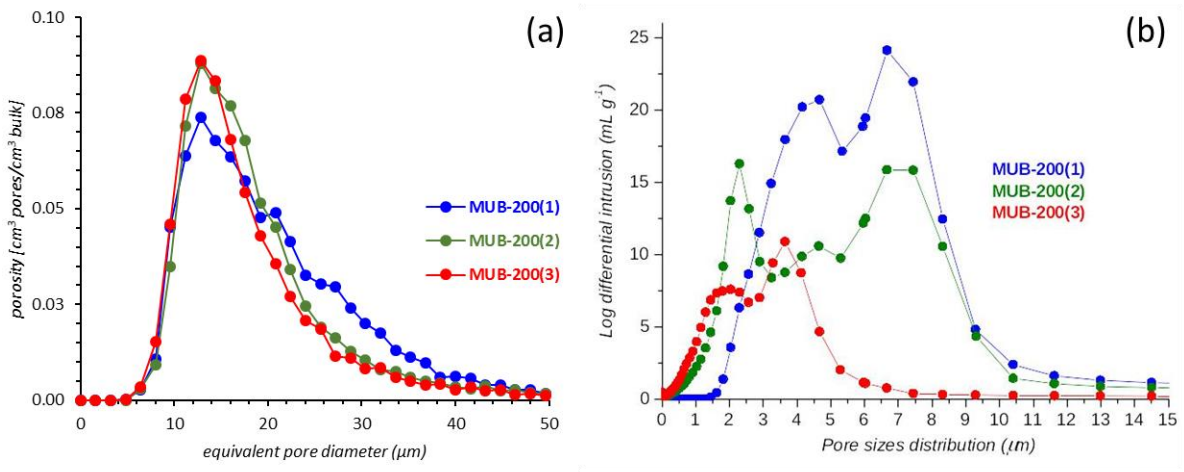

Figure 2. Pore size distributions obtained through (a) X-ray imaging and (b) mercury porosimetry. MUB-200(1) blue dots, MUB-200(2) green dots and MUB-200(3) red dots.

When considering the Figure 2, we have first to underline that the pore size distribution as obtained by X-ray imaging is sensitive to the cell bodies, while the one obtained with mercury porosimetry is largely determined by the dimensions of the throats connecting the different cells. It is therefore unsurprising that the mean (cell) diameters estimated by X-ray imaging are systematically larger than the (throat) diameters obtained from porosimetry. As it is the case for Si(HIPE) materials,[48] the throats are rather polydisperse in diameters ranging from 1.5 to 10 µm with a tendency of expressing a bimodal character (Fig. 2 (b)). The cell diameters are rather unimodal, with diameters ranging from 5 to 50 µm, the most frequent diameter being around ~13 µm. We can notice the tendency of both the cell and the throat diameters to slightly diminish while increasing the P25 nanoparticle contents from the MUB-200(1) to the MUB200(3) materials, signifying a decrease of the coalescence process. Beyond the cell junction sizes, mercury porosimetry is also addressing the materials' bulk density (Table 1). From the bulk densities obtained through mercury infiltration experiments and skeleton densities obtained though helium pycnometry it is possible calculating the materials' percentage of porosity (eq. 1).

$$\% \text{ Porosity} = [1- (\text{Bulk density}/\text{skeleton density})] * 100 \quad (1)$$

Table 1. Bulk density measured by mercury, skeleton density measured by helium pycnometry, % porosity calculated porosity using equation (1). BET nitrogen physi-sorption data, and BJH surface area calculated from the adsorption curves.

Sample	Porosity (%)	Skeleton density ($g\ cm^{-3}$)	Bulk density ($g\ cm^{-3}$)	BET surface area ($m^2\ g^{-1}$)	BJH surface area ($m^2\ g^{-1}$)
Si(HIPE)	96± 2%	2.22± 0.05	0.085± 0.005	930± 30	500± 30
MUB-200(1)	97± 2%	2.44± 0.05	0.083± 0.005	1035± 30	490± 30
MUB-200(2)	96± 2%	2.53± 0.05	0.105± 0.005	930± 30	590± 30
MUB-200(3)	96± 2%	3.01± 0.05	0.130± 0.005	690± 30	430± 30

The materials skeleton and bulk densities are increasing with the P25 nanoparticle contents while addressing a constant % of porosity around 96 % (Table 1). We can say that the P25 nanoparticles favour a decrease of the oil droplet diameters compensated with an increase of the droplet numbers. In brief, the increasing nanoparticle contents, through the increased viscosity, is increasing the shear addressed to the droplets and thereby is increasing the droplet numbers while allowing at the same time stabilizing the higher number of native interfaces. In order to estimate the P25 Degussa repartition within the siliceous matrices we first performed TEM. Indeed, even at low titania nanoparticle contents (MUB-200(1)), the TiO_2 nanoparticles are limiting the transmission effect resulting in rather blurry pictures where depicting the TiO_2 nanoparticle repartition within the silica matrices was not possible. In order to circumvent this penalty we have performed X-ray 3D microtomography investigations. Figure 3 depicts digital cuts through the volumes of interest already depicted in Fig. 1 (b-d) for the three materials of the MUB-200(x) series. The grey scale of the images in the top row is roughly proportional to the mass attenuation coefficient of the dominant material in each (800 nm x 800 nm) pixel, it ranges from dark for the air in the pores, over grey for the matrix to white for the TiO_2 nanoparticles. To guide the eye, Fig. 3 (d-f) represent the same images, yet in false colour where the TiO_2 nanoparticles are highlighted in yellow. Three observations can be made. Firstly, the TiO_2 content clearly increases from MUB-200(1) to

MUB-200(3), with the biggest increase occurring between MUB-200(1) and MUB-200(2). Secondly, the TiO_2 nanoparticles are randomly spread throughout the material matrix. As the depicted plane is deeply embedded in the bulk of the material (at least 1 mm from the surface) and considered representative, this proves that the proposed one-pot synthesis leads –at least qualitatively- to a homogeneous nanoparticle distribution. Combined with the high porosity of the samples (Table 1), this yields a cloud of nanoparticles supported by a low density matrix and, as will be shown further (Section 3.4), accessible to light. As a final observation, we notice the presence of some larger white (Fig. 3 (a-c)) or yellow (Fig. 3 (d-f)) patches, revealing that some of the TiO_2 particles clustered together during syntheses.

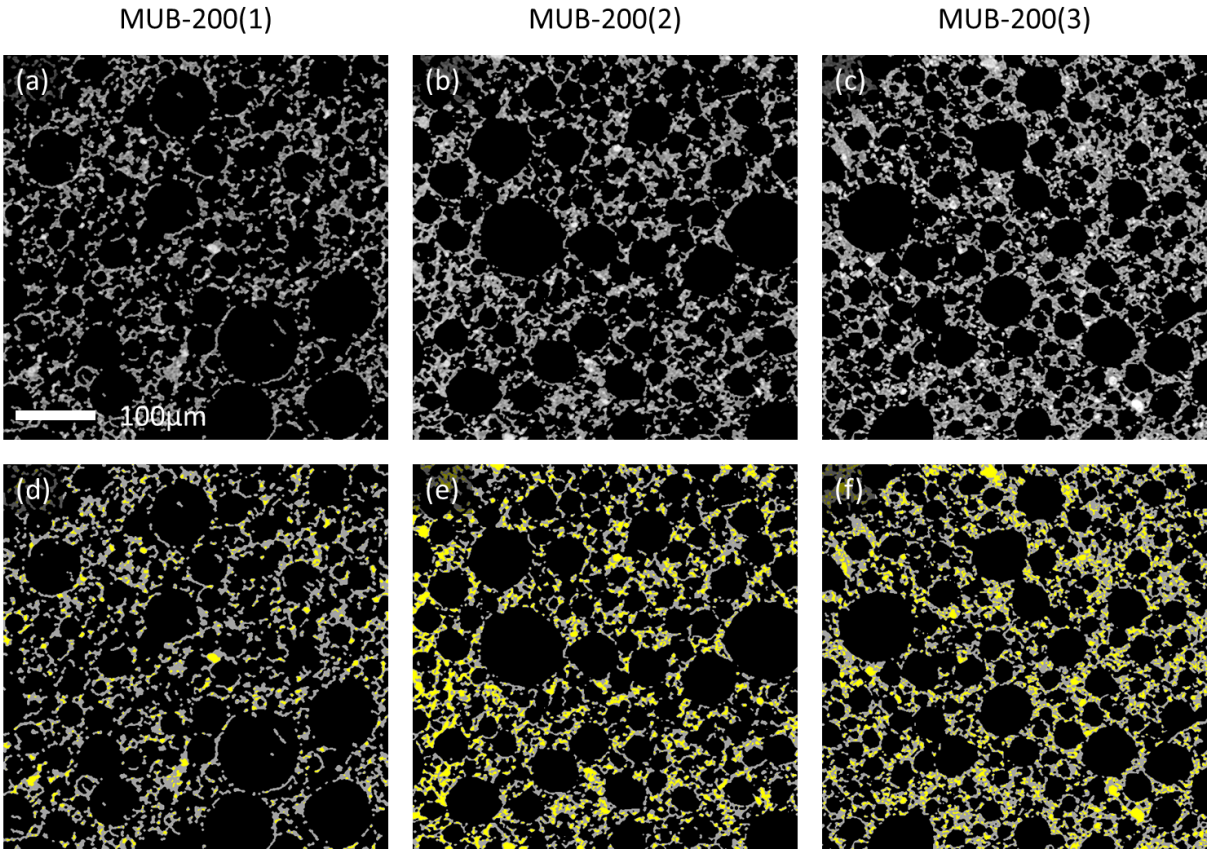

Figure 3. (a-c) Digital cut through the 3D X-ray tomographic datasets for the three materials of the MUB-200(x) series. (d-f) false colour image of the same image plane where black represents pores, grey represents the SiO_2 matrix and yellow the TiO_2 inclusions.

Materials characterization at the mesoscopic length scale

Table 1 is also depicting the materials specific surface area at the mesoscopic length scale. We first notice a small increase of the BET and BJH surface areas while adding P25 nanoparticles from the Si(HIPE), being free of P25 nanoparticles, to the MUB-200(1). The nitrogen physi-sorption isotherms are depicted on Fig. 4.

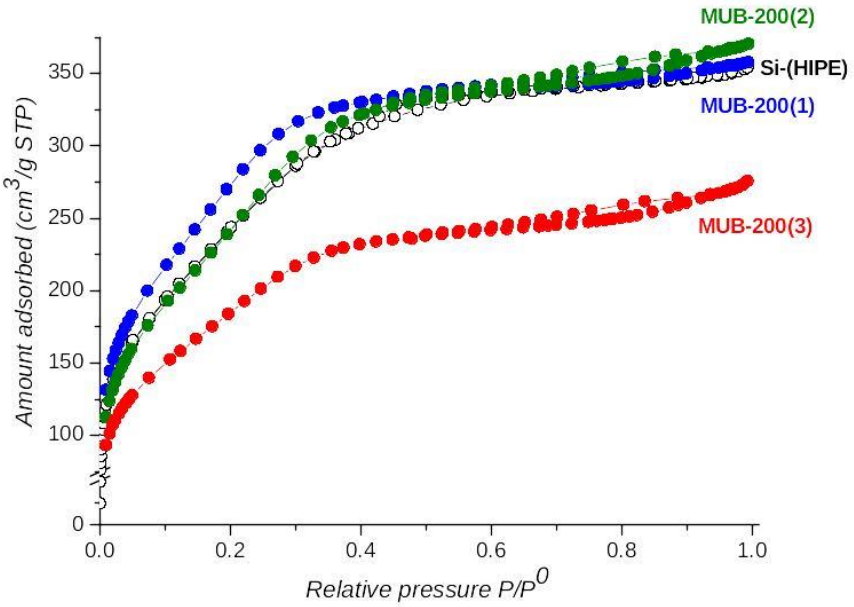

Figure 4. Gas physisorption measurements, N_2 adsorption-desorption curves.

We can always observe nitrogen adsorption at low relative pressure signifying the presence of micropores (pore sizes below 2 nm), a weak hysteresis at high relative pressure that depicts a certain degree of mesoporosity (pore sizes between 2 and 50 nm). Also at high relative pressure (above 0.8) we can see a N_2 up-take, feature that is announcing the macroporosity. Aside, a slight increase of the BET surface area from the Si(HIPE) to the MUB-200(1) has been found (Table 1). This small increase of surface area being certainly induced by the titania nanoparticle external surfaces. Considering the whole MUB-200(x) series, the BET surface area is decreasing from the MUB-200(1) to the MUB-200(3) (Table 1) certainly because the small increase of the surface area offered by the titania nanoparticles does not compensate the increase of the wall skeleton densities, the BET being provided in

square meter per gram. In order to assess further the mesoscopic voids organization, Small Angle X-ray Scattering (SAXS) experiments have been performed. As shown in Fig. 5 (a), the smaller wave-vector part of the scattering intensity data exhibits the expected power-law decay with exponent -4 (Porod's law)[59] for the reference Si(HIPE) only. Trying to model the initial decay by power laws, significantly less negative exponents are found for MUB-200(1), namely -3.2, and MUB-200(2) or MUB-200(3), with values about -2.5 for these last two samples. As Porod's law is characteristic of clear-cut, locally planar interfaces—here separating an "outer" empty medium (air) from an "inner" filled medium (silica-rich walls)—, this suggests that interfaces (still locally planar at scales probed by X-rays) have been broadly roughened by the presence of bumps of titania nanoparticles on the level surface of silica walls. In order to enhance the visibility of structural features at mesoscopic scales, the initial intensity decay is normalised out in Fig. 5 (b), where a customised modification of the standard Porod representation, namely $q^{-\nu}$. *I* plotted as a function of *q* in linear scales, has been used. One or three peaks clearly emerge in this representation. The peak marked by a star (*)–the only one observed for Si(HIPE)–is commonly assigned to the remains of the TTAB concentrated worm-like micellar phase / 2D hexagonal phase used during the material syntheses. This peak corresponds to a characteristic scale $2\pi/q^*$ in the order of 3.4 nm for Si(HIPE), with minute effects of P25 nanoparticles as it reaches at most 3.5 nm for MUB-200(2) or MUB-200(3). More significant, two additional peaks (marked with single and double daggers), characterise the presence of P25 nanoparticles since they are not observed with Si(HIPE). They cannot be simply ascribed to, *e.g.*, dense aggregates of P25 nanoparticles because the centre-to-centre distance in such a hypothetical structure would then be in the order of the particle diameter, namely about 20 nm, a value far too large compared to $2\pi/q^\dagger$ – about 6.6 nm. A less naive interpretation would be invoking an interplay between (higher order) structure factor peaks in dense clusters of nanoparticles and form factor oscillations, as

the latter exhibit humps at locations close to (among other values) $q^{\dagger}$ and $q^{\ddagger}$ for a nanoparticle diameter equal to 20 nm. A detailed mechanism for wiping out the other form factor oscillations, the one at about 0.12 $Å^{-1}$ for instance, is however lacking. Aside, as part of the TTAB tension-active molecules favours the P25 nanoparticle dispersion, we may not excluded that the TTAB/water phase diagram evolves toward phases expressing TTAB lower concentrations.

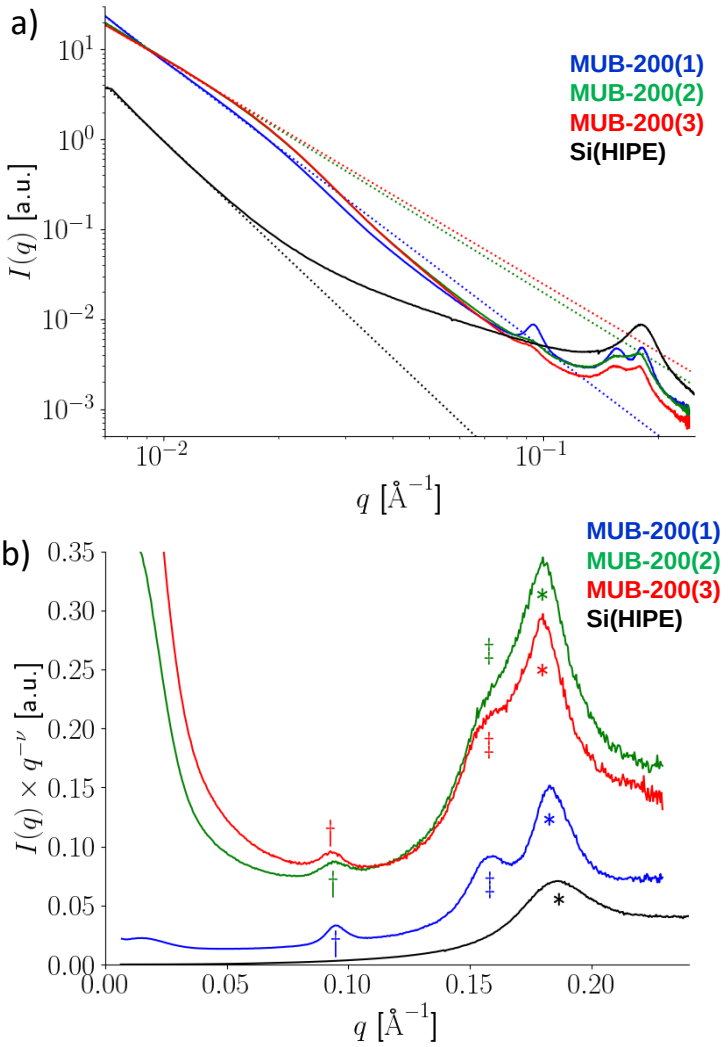

Figure 5. (a) Small-angle scattering intensities (double logarithmic scale) for the reference Si(HIPE) sample (black), and the three MUB-200(1) (green), MUB-200(2) (blue) and MUB-200(3) (red) samples. The coloured dotted lines correspond to power-law decaying intensities with exponents ν close to -4 (Porod's law) for Si(HIPE) , but steadily increasing with titania concentration, respectively -3.2, -2.6 and -2.5 from MUB-200(1) to MUB-200(3). (b) Same as (a), but in the so-called "Porod representation" $q^{\nu}.I$ emphasizing mesoporous scales. The coloured symbols mark for each sample the locations in reciprocal space of characteristic structural peaks—only one is observed for Si(HIPE), but three in the case of MUB-200 samples. Peak positions: about 0.094, 0.16 and 0.18 $Å^{-1}$ for $q^{\dagger}$, $q^{\ddagger}$ and q^{*} respectively.

Materials characterization at the microscopic length scale

At the microscopic length scale Wide Angle X-ray Scattering (WAXS) reveals the biphasic nature of the P25 titania nanoparticles where the two anatase and rutile allotropic forms can be distinguished (Fig. 6).

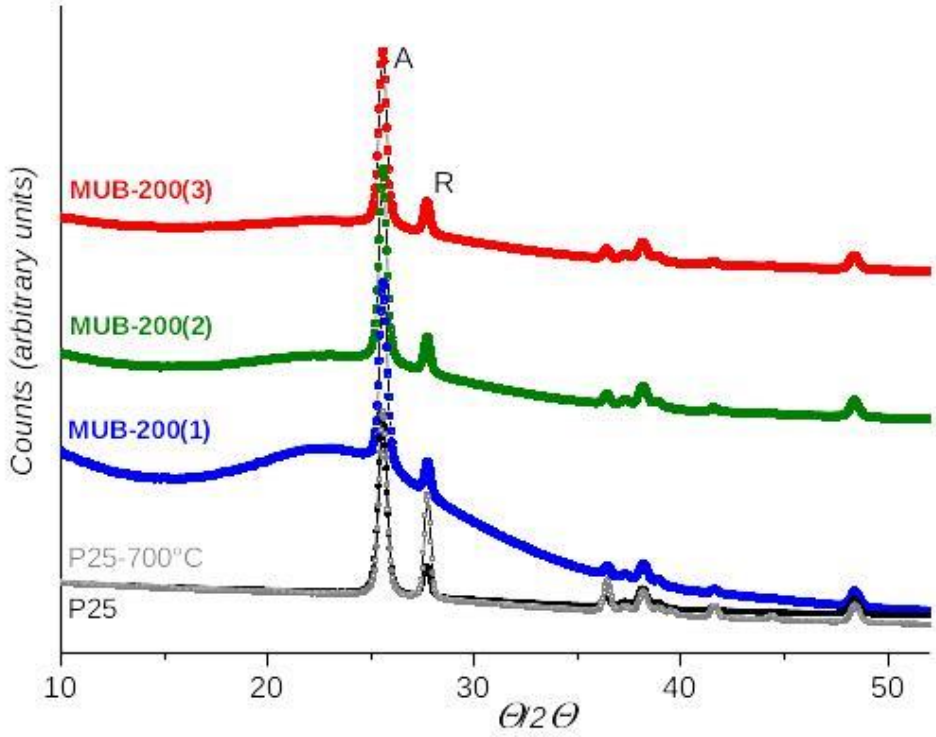

Figure 6. Wide angle X-ray Scattering (WAXS) investigations. Black P25 Degussa, light gray P25 Degussa treated at 700 °C, blue MUB-200(1), green MUB-200(2), red MUB-200(3).

We can notice that the unconfined P25 nanoparticles undergo a phase transition from the anatase to rutile while applying a 6 h thermal treatment at 700 °C in air. This allotropic phase transition is completely cancelled when the P25 nanoparticles are embedded within the silica matrices. This phenomenon is kind of unexpected as during the liquid-phase hydrolysis in the excess of water, water molecules formed a thin film on the modified matrix surface and easily cleaved the Si-O-Ti bonds to afford discretized SiO_2 and TiO_2 phases.[60] Despite, at the molecular level, we have already observed such forbidden silica-titania interaction where TiO_2 was heterogeneously grown at the silica wall surface,[46] we mentioned *i.e.* "*a pseudo epitaxial phenomenon demonstrating that..., the Si-O-Ti bonds at the silica/titania interfaces are not cleaved, as the amorphous silica network can hinder the* TiO_2 *crystallization upon*

thermal treatment, when no pre-hydrolyzed sols are employed". Recently it has been shown that the TiO_2 crystal growth is controlled by the growth of the particle interfaces leading both to an increase of the phase transition temperature and activation energy.[61] In the present case not only the anatase to rutile allotropic change is hindered at the molecular level, but it is the whole P25 Degussa nanoparticles when confined within the silica matrices that do not depicted the anatase to rutile phase transition, even during a 7 h treatment at 700 °C (Fig. 5). It means that the silica matrices due to its amorphous character is here still locking the P25 allotropic phase transition from the metastable anatase to the more thermodynamically stable rutile phase, whatever the P25 Degussa nanoparticle contents, from the lowest P25 content with the MUB-200(1) to the highest one with the MUB-200(3). This behavior is not observed when the P25 nanoparticles are not confined. HR-TEM investigations show that the titania nanoparticles are indeed completely embedded within the siliceous matrices through continuous SiO_2/TiO_2 interfaces, where some (101) lattices of a tetragonal anatase crystal can be distinguished (Figure S2). This feature is indeed very important, as the intrinsic anatase-rutile heterojunction is thereby maintained during the MUB-200(x) series syntheses, opening the path for very effective VOCs photo-oxidation properties. Still at the microscopic length scale, elemental coupled with Thermo-Gravimetric Analyses (TGA) analyses have been performed to provide the porous materials' stoichiometry (Table 2).

Table 2. Elemental analysis data and TGA addressing material Molar Weight (MW) and stoichiometry. *The H_2O wt% have been found by TGA under air under a heating rate of 5°C min^{-1}. The TGA can be found within the supplemental section (Fig. S3). Elemental analyses have been performed using ICP for titanium and silicon atoms wt% determinations.

Sample	Ti wt% Found	Ti wt% Cal	Si wt% Found	Si wt% Cal	H_2O wt% Found*	H_2O wt% Cal	MW g mol^{-1}	Proposed Stoichiometry
MUB-200(1)	8.40	8.31	30.50	30.41	12.65	12.76	91.68	$(TiO_2)_{0.16}(SiO_{1.6}(OH)_{0.8})_{1.0}.0.65H_2O$
MUB-200(2)	18.71	18.82	26.07	26.21	6.10	6.23	107.40	$(TiO_2)_{0.42}(SiO_{1.6}(OH)_{0.8})_{1.0}.0.38\ H_2O$
MUB-100(3)	23.72	24.06	22.62	22.35	6.11	6.24	125.28	$(TiO_2)_{0.63}(SiO_{1.6}(OH)_{0.8})_{1.0}.0.43\ H_2O$

When considering Table 2 we can notice that the TiO_2 content is increasing within the as-synthesized MUB-200(x) series consequently of increasing the amount of P25 Degussa nanoparticles employed during the syntheses, from the MUB-200(1) to the MUB-200(3). Also the materials' hydration is decreasing while increasing the TiO_2 nanoparticle contents. At first hand, we may say that this characteristic is just an effect of the lowering H_2O wt%, as increasing the TiO_2 content within the materials. On a second hand, when looking at the material's stoichiometry we can notice that the water content is decreasing from 0.65 moles of water per silica for the MUB-200(1) to 0.38 and 0.43 mole of water per mole of silica respectively for the MUB-200(2) and MUB-200(3) (Table 1). It means that the materials hydration is decreasing while increasing the P25 nanoparticles content, feature that is very clear when looking at the TGA experiments while focusing at the abrupt weight loss occurring before 100 °C (Figure S3). This feature shows that due to its intrinsic hydrophilic-hydrophobic balance[62] the non-irradiated P25 TiO_2 nanoparticles render the catalysts intrinsically less hydroscopic.

Photonic investigations

In order to step forward to the determination of the samples 3D-photo-efficiency, we aim here to determine their transmission properties. These provide the transport mean free path l_t and the absorption length l_a which, in the standard diffusion model,[63] relate to the penetration depth of light in the sample. When considering diffusion, the situation we face with the MUB-200(x) series is that it strongly departs from the single scattering regime governed by Beer-Lambert's law, with a transmission given $T = e^{-L/l_{sc}}$, where L is the thickness of the sample and l_{sc} is the scattering mean free path, *e.g.* the mean length between successive scatterers. In the multiple scattering regime, as we have here with a "flipper-like" type of motion, where the resonators' role is played by photons bouncing on the walls surrounding the voids, the transmission is governed by Ohm's law, $\propto \frac{l_{sc}}{L}$, while considering a non-absorbing materi-

al. In the presence of absorption, a more complex behavior is expected, which is governed by the standard diffusion model.[47] Figure 7 shows both l_t as a function of wavelength obtained for the MUB-200(x) series (a) and the all-angle integrated forwards scattering measurements performed on the MUB-200(3) as a function of thickness of the investigated samples and wavelength of the excitation light (b).

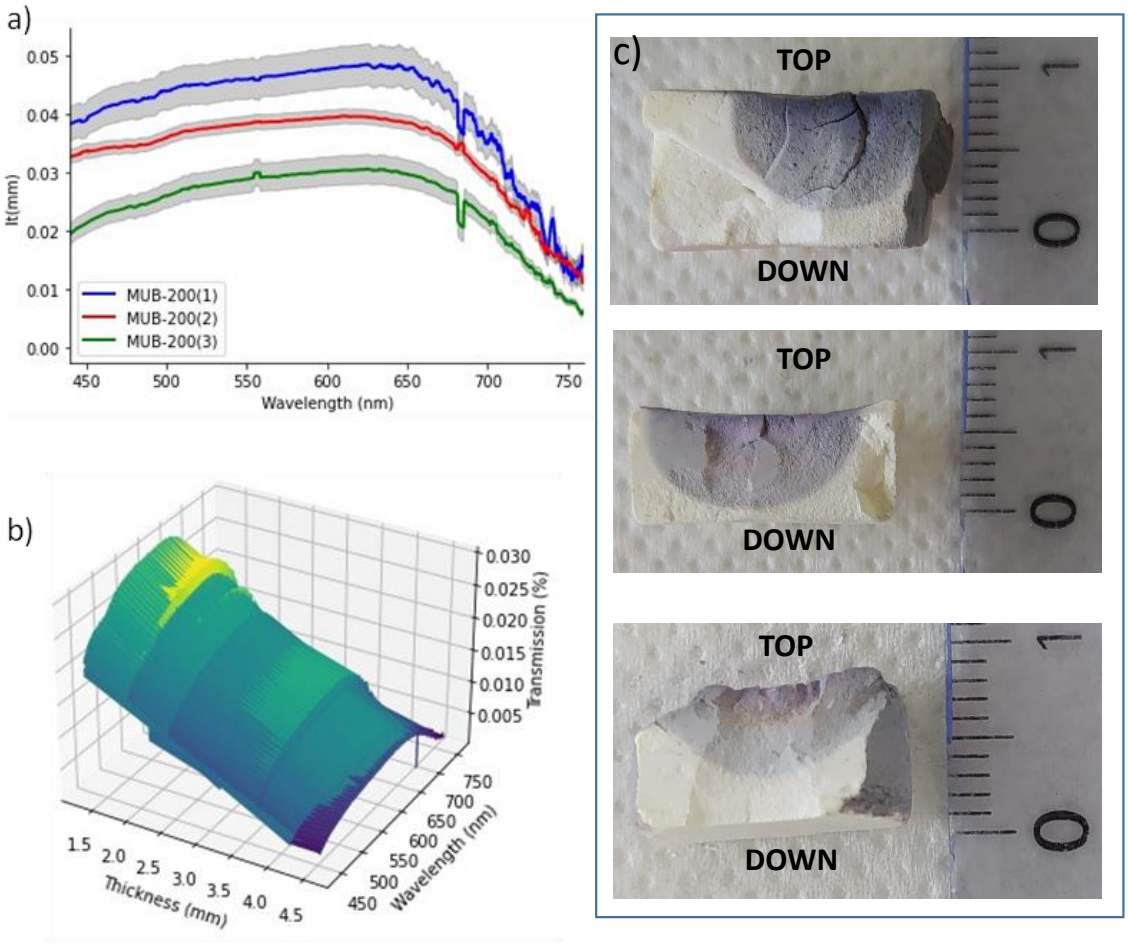

Figure 7. (a) Spectra of the transport mean free paths for the MUB-200(1) (blue), MUB-200(2) (green), MUB-200(3) (red) determined from a fit of the transmission data to Equation (S1). (b) Forwards integrated transmission as a function of excitation wavelength and thickness of the various samples for the MUB-200(3). (c) Gold photoreduction within MUB-200(x) (top MUB-200(1) ; middle MUB-200(2) and bottom MUB-200(3)) as a red-rubbish colored probe. A gold salt solution of 10^{-2} M was prepared from $KAuCl_4$ in 2-propanol. MUB-200(x) materials were then impregnated under vacuum in a desiccator. Once dried, Chloroaurate ions were reduced during 1 h into gold zerovalent nanoparticles under UV irradiation provided by a metal halide lamp (40 W cm^{-2} – λ = 280–450 nm) located 7 mm above the monolith surfaces by the mean of optical fiber waveguide.

The all-angle integrated forwards scattering measurements have been fitted owing to the stationary solution of the diffusion including absorption, which yields l_t and l_a.[47,52,63] As shown in Fig. 7 (b), an approaching 1/L dependence of the transmission can be observed for

all wavelengths. The departure from this trend is due to (mainly) TiO_2 absorption, which is considered by the standard diffusion model. The fitted transport mean free paths at maxima of the spectra (Fig. 7 (a)) decrease from $l_t = 0.05$ to 0.03 *mm* while the TiO_2's content of the respective MUB-200(x) series increases. This is a well-expected behavior since formed TiO_2 particles deposit on and into the walls separating the droplets, thus modifying their texture and density. As depicted in Table 1, the larger amount of TiO_2 is introduced in the materials, the larger is the density of the walls and the smaller is the mean size of the voids, both effects inducing a reduction of the transport mean free path. These are the consequences of the large wall shrinkage and skeleton density increase during polycondensation for the materials bearing the larger amount of titania. For these three types of samples, the absorption length (2-3 mm, not shown) was furthermore found to be of the same order of magnitude than the thicknesses of the samples themselves, making their determination highly error prone. In order to visually witness the bulk behavior of these photoreactors we have operated a gold salt photoreduction. Here we have first infiltrated the MUB-200(x) series with a $KAu^{III}Cl_4$ salt while performing the Au^{III} photoreduction toward Au°, where the change of oxidation state promotes a color change from pale yellow to red rubbish ascribed to the Plasmon band of the zero-valent native gold nanoparticles.[46] The results, depicted within the Fig. 7 (c), are addressing a photon penetration depth around 6 mm. Within the limit of our knowledge this photoefficiency over a thickness of 6 mm has never been reached to date, depicting thus a real 3D behavior when acting with light as a photonic scavenger.

VOCs Photo-abatement efficiency

The MUB-200(x) series photocatalytic properties were studied in dynamic mode (a single pass over the catalysts (Fig. S1). Initially acetone was used as a model VOC. Acetone has been extensively employed for probing gas-phase efficiency of various photocatalytic media due to its easy mineralization without large formation of gaseous intermediates.[64–67] All

experiments were carried out under identical conditions: initial concentration of 140 ppmV in acetone, 40 % RH and acetone saturation of the material in the dark, then the lamps were switched on. In these experimental conditions it may be assumed that the contact time of VOC with photocatalyst is around 1 s (ratio between flow rate and volume of photocatalyst). Figure 8 shows the results obtained in a typical photocatalytic experiment with the MUB-200(1) material.

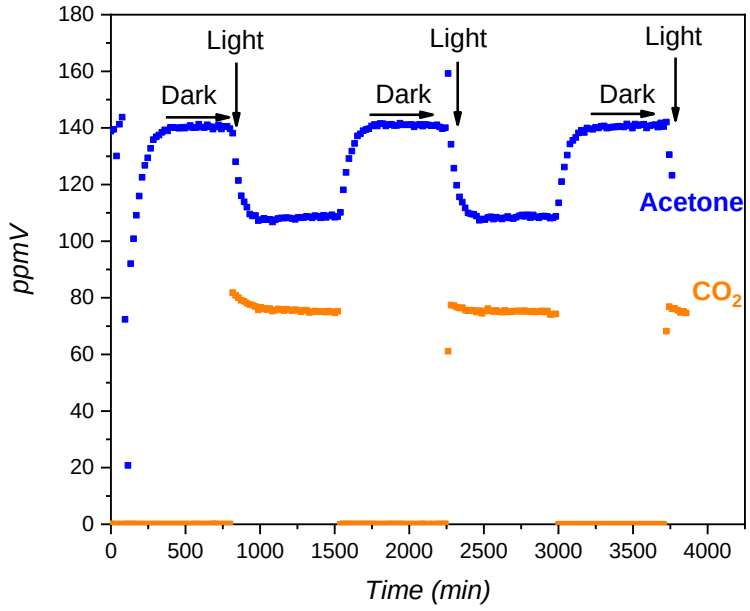

Figure 8. Acetone and CO_2 concentrations against time during a photocatalysis experiment with MUB-200(1) material. The dark periods correspond to the saturation of the material with acetone.

The first phase (adsorption in the dark) corresponds to the adsorption of acetone on the material. As soon as the lamps are switched on, a decrease in the acetone concentration (-34 ppmV) and an increase in the CO_2 concentration (+83 ppmV) are observed, reflecting the mineralization of acetone. CO_2 is the main photoproduct detected in the gas flow even if low concentrations of acetaldehyde (less than 50 ppb) are also detected along the irradiation phase. If we consider that one mole of acetone can produce three moles of CO_2, we can roughly estimate the mineralization rate at 79 %. These concentrations are stable over time, which means that a photo-stationary state is obtained: the number of moles of acetone adsorb-

ing on the material is equal to the number of moles of photo-oxidized acetone upon irradiation. The adsorption/photo-oxidation cycle can be repeated several times without loss of efficiency. Table 3 gathers the results obtained for the whole MUB-200(x) series. It may be recalled that TiO_2 stoichiometries are 0.16, 0.42 and 0.63 respectively for MUB-200(1), MUB-200(2) and MUB-200(3). Some conclusions can be drawn from these results. First, all materials offer approximately the same adsorption capacity (about 0.4 mmol g^{-1} of acetone on average). The presence of TiO_2 in the structure does not seem to influence the acetone adsorption in a significant way. The value obtained is significantly lower than those with other types of adsorbents (mesoporous silica[68] activated carbons[69]). Nevertheless it should be underlined that the operating conditions were not optimized for adsorption in this study and a high adsorption capacity does not prejudge a material photoactivity high efficiency. For instance, the commercial material Quartzel®, despite low acetone absorption, is very effective towards acetone mineralization.[70]

Table 3. Photocatalytic activity of the different materials toward the mineralization of acetone.* % acetone adsorbed = mass of acetone adsorbed/mass of the monolith. ** photo-oxidized acetone = $[acetone]_{dark}$-$[acetone]_{irradiated}$ *** % mineralization = $[CO_2]_{exp}/(3*[acetone]_{photooxidased})*100$.

Entry	Material	Monolith	Mass (g)	Height (mm)	Acetone adsorbed (mg)	Acetone adsorbed % (mg/g)*	Photooxidized acetone (ppmV)**	CO_2 product (ppmV)	Mineralization %***
1	MUB-200 (1)	TiO_2 0,3 A	0.142	4.29	3.3	24	34	83	79
2	MUB-200(2)	TiO_2 0,8 A	0.154	4.11	3.5	23	32	74	77
3	MUB-200(3)	TiO_2 1,2 A	0.244	4.29	5.4	22	32	73	75
4	MUB-200 (1)	TiO_2 0,3 B	0.101	3.7	3.2	23	30	65	72
5	MUB-200(1)	TiO_2 0,3 C	0.146	3.85	3.5	24	19	44	77
6	MUB-200(1)	TiO_2 0,3 C	0.135	3.02	3.1	23	17	42	80
7	MUB-200(1)	TiO_2 0,3 C	0.101	2.52	1.9	19	17	38	75

Secondly, despite a very different TiO_2 stoichiometry, the three materials of approximatively equal height, show roughly equivalent photoactivity. Photo-oxidized acetone be-

tween 32 and 34 ppmV offers a mineralization ratio between 75 and 79 % (Table 3). This could mean that the number of photoactivable sites are identical into the three materials, i.e. light can activate as many TiO_2 particles in MUB-200(1) as in MUB-200(3). This result seems to be consistent with the photonic results presented in the previous paragraph where it was shown that the fitted transport mean free paths decrease while the TiO_2's content of the respective MUB-200(x) series increases. Entries 5, 6 and 7 of Table 3 show the influence of the height (volume) of the monolith on its properties. In these experiments, the same monolith was sanded so that its height decreased. It can be seen that the mass and the proportion of acetone adsorbed are proportional to the height (volume) of the monolith. Similarly, the highest photoactivity (concentration of acetone ablated and concentration of CO_2 formed) is obtained with the highest monolith height (volume), also in line with a 3D-photoactive material. These experimental results validate the fact that these materials, bearing a 3D-photoactivity, open the path for air purification operating with self-standing porous monolith-type materials that are much easier to handle than powders. This is a first obvious advantage whereas usual photocatalytic materials (based on TiO_2 or silica/TiO_2) are formulated either with slurry deposited onto a support or non-porous ceramic type materials which can act only as 2D materials. To the best our knowledge, this is the first example of photoactive SiO_2/TiO_2 monoliths offering heterogeneous photoinduced air-treatment at the gas-solid interface. Indeed if the preparation of TiO_2/SiO_2 monoliths has been well described, their photoactivity has only been studied in solution by the study of dyes decoloration.[71,72] The second very important advantage is indeed "geometric". As working now within the volume of the photocatalysts and not only on their outer surface, while providing up-grated photoefficiency (Fig. 7, Table 3), the photocatalytic systems could be miniaturized, offering the potential towards air indoor treatment within vehicles/homes while limiting drastically the associated encumbrance or foot print penalty. This specificity of acting in "volume" rather than on "surface" while limiting foot print penalty is

indeed a dramatic advance because hearth population is growing exponentially and the action of minimizing foot print penalty while considering photo-reactors is a sine qua non scenario (fundamental endeavor) to preserve precious agricultural soils (and associated food). This point being valid for VOCS photo-abatements, CO_2 photo-reduction, water splitting, DSSCs and so forth.

CONCLUSIONS

While combining sol-gel chemistry, P25 nanoparticles and the physical chemistry of complex fluids, emulsion-based cellular self-standing nano-particulate ceramics have been generated for the first time and labelled as the MUB-200(x) series. The synthetic path is rather simple where final materials' shapes can be tuned on demand offering a certain modularity. The native ceramic self-standing foams are bearing specific surface are around 700-1000 m^2 g^{-1} while maintaining the anatase/rutile crystalline phase ratio equals to the starting P25 Degussa nanoparticles, despite a thermal treatment at 700 °C during 7 h. Photonic investigations correlated with the foams' morphologies suggest that the larger amount of TiO_2 is introduced, the higher is the walls' density, the smaller is the mean size of the void macroscopic diameters, the smaller is photon transport mean free path (l_t). The photocatalytic properties of the MUB-200(x) series, studied in a "dynamic flow through" configuration show that, the highest photoactivity (concentration of acetone ablated and concentration of CO_2 formed) is obtained with the highest monolith height (volume), while providing an average of 75 % mineralization. These photocatalytic results validate the fact that these materials, are bearing a 3D-photoactivity, opening thereby both the path for air purification operating with self-standing porous 3D-monolith-type materials (and not flowable nano-powder anymore), and secondly

indoor air-treatment within vehicles/homes while limiting drastically the associated encumbrance as acting in volume and not only on outer surfaces anymore.

Associated contents (SI)

The Supporting Information is available free of charge at https://pubs.acs.org/doi/xxxxxxxxxx.
Flow through photocatalytic reactor scheme, HR TEM investigations of MUB-200(3) at the titania-silica interface, TGA in air of the MUB-200(x) series, (PDF)

Author contributions

The manuscript was written through contributions of all authors. All authors have given approval to the final version of the manuscript.

Acknowledgements

The authors acknowledge funding from the University of Bordeaux-IDEX through the "*Post Petroleum Materials grands programmes de recherche*". We wish to thank Sonia Buffière (Placamat-Université de Bordeaux) for the HR-TEM image acquisitions and Ahmed Bentaleb (CRPP) for the SAXS data acquisitions.

References

(1) Yu, B. F.; Hu, Z. B.; Liu, M.; Yang, H. L.; Kong, Q. X.; Liu, Y. H. Review of Research on Air-Conditioning Systems and Indoor Air Quality Control for Human Health. *International journal of refrigeration* **2009**, *32*, 3–20.
(2) Cheng, Y.-H.; Lin, C.-C.; Hsu, S.-C. Comparison of Conventional and Green Building Materials in Respect of VOC Emissions and Ozone Impact on Secondary Carbonyl Emissions. *Building and Environment* **2015**, *87*, 274–282.
(3) Guieysse, B.; Hort, C.; Platel, V.; Munoz, R.; Ondarts, M.; Revah, S. Biological Treatment of Indoor Air for VOC Removal: Potential and Challenges. *Biotechnology advances* **2008**, *26* (5), 398–410.
(4) Bahri, M.; Haghighat, F. Plasma-B Ased Indoor Air Cleaning Technologies: The State of the Art-R Eview. *CLEAN–Soil, Air, Water* **2014**, *42*, 1667–1680.
(5) Zhang, G.; Xiong, Q.; Xu, W.; Guo, S. Synthesis of Bicrystalline TiO2 Supported Sepiolite Fibers and Their Photocatalytic Activity for Degradation of Gaseous Formaldehyde. *Applied clay science* **2014**, *102*, 231–237.
(6) Yang, L.; Liu, Z.; Shi, J.; Hu, H.; Shangguan, W. Design Consideration of Photocatalytic Oxidation Reactors Using TiO2-Coated Foam Nickels for Degrading Indoor Gaseous Formaldehyde. *Catalysis Today* **2007**, *126*, 359–368.
(7) Zhong, L.; Haghighat, F.; Lee, C.-S.; Lakdawala, N. Performance of Ultraviolet Photocatalytic Oxidation for Indoor Air Applications: Systematic Experimental Evaluation. *Journal of hazardous materials* **2013**, *261*, 130–138.
(8) Farhanian, D.; Haghighat, F. Photocatalytic Oxidation Air Cleaner: Identification and Quantification of by-Products. *Building and Environment* **2014**, *72*, 34–43.
(9) Gaya, U. I.; Abdullah, A. H. Heterogeneous Photocatalytic Degradation of Organic Contaminants over Titanium Dioxide: A Review of Fundamentals, Progress and Problems. *Journal of photochemistry and photobiology C: Photochemistry reviews* **2008**, *9*, 1–12.

(10) Tseng, T. K.; Lin, Y. S.; Chen, Y. J.; Chu, H. A Review of Photocatalysts Prepared by Sol-Gel Method for VOCs Removal. *International journal of molecular sciences* **2010**, *11*, 2336–2361.
(11) Ji, J.; Xu, Y.; Huang, H.; He, M.; Liu, S.; Liu, G.; Xie, R.; Feng, Q.; Shu, Y.; Zhan, Y. Mesoporous TiO2 under VUV Irradiation: Enhanced Photocatalytic Oxidation for VOCs Degradation at Room Temperature. *Chemical Engineering Journal* **2017**, *327*, 490–499.
(12) Tejasvi, R.; Sharma, M.; Upadhyay, K. Passive Photo-Catalytic Destruction of Air-Borne VOCs in High Traffic Areas Using TiO2-Coated Flexible PVC Sheet. *Chemical Engineering Journal* **2015**, *262*, 875–881.
(13) Lopes, F. V.; Monteiro, R. A.; Silva, A. M.; Silva, G. V.; Faria, J. L.; Mendes, A. M.; Vilar, V. J.; Boaventura, R. A. Insights into UV-TiO2 Photocatalytic Degradation of PCE for Air Decontamination Systems. *Chemical engineering journal* **2012**, *204*, 244–257.
(14) Galliano, S.; Bella, F.; Gerbaldi, C.; Falco, M.; Viscardi, G.; Grätzel, M.; Barolo, C. Photoanode/Electrolyte Interface Stability in Aqueous Dye-sensitized Solar Cells. *Energy Technology* **2017**, *5*, 300–311.
(15) Bella, F.; Muñoz-García, A. B.; Meligrana, G.; Lamberti, A.; Destro, M.; Pavone, M.; Gerbaldi, C. Unveiling the Controversial Mechanism of Reversible Na Storage in TiO2 Nanotube Arrays: Amorphous versus Anatase TiO2. *Nano Research* **2017**, *10*, 2891–2903.
(16) Bella, F.; Pugliese, D.; Zolin, L.; Gerbaldi, C. Based Quasi-Solid Dye-Sensitized Solar Cells. *Electrochimica Acta* **2017**, *237*, 87–93.
(17) Hou, X.; Zhou, J.; Huang, S.; Ou-Yang, W.; Pan, L.; Chen, X. Efficient Quasi-Mesoscopic Perovskite Solar Cells Using Li-Doped Hierarchical TiO2 as Scaffold of Scattered Distribution. *Chemical Engineering Journal* **2017**, *330*, 947–955.
(18) Yu, J.; Wang, W.; Cheng, B.; Su, B.-L. Enhancement of Photocatalytic Activity of Mesporous TiO2 Powders by Hydrothermal Surface Fluorination Treatment. *The Journal of Physical Chemistry C* **2009**, *113*, 6743–6750.
(19) Zeng, L.; Lu, Z.; Li, M.; Yang, J.; Song, W.; Zeng, D.; Xie, C. A Modular Calcination Method to Prepare Modified N-Doped TiO2 Nanoparticle with High Photocatalytic Activity. *Applied Catalysis B: Environmental* **2016**, *183*, 308–316.
(20) Feng, Y.; Li, L.; Ge, M.; Guo, C.; Wang, J.; Liu, L. Improved Catalytic Capability of Mesoporous TiO2 Microspheres and Photodecomposition of Toluene. *ACS applied materials & interfaces* **2010**, *2*, 3134–3140.
(21) Ferrari-Lima, A. M.; Marques, R. G.; Gimenes, M. L.; Fernandes-Machado, N. R. C. Synthesis, Characterisation and Photocatalytic Activity of N-Doped TiO2–Nb2O5 Mixed Oxides. *Catalysis Today* **2015**, *254*, 119–128.
(22) Burns, A.; Hayes, G.; Li, W.; Hirvonen, J.; Demaree, J. D.; Shah, S. I. Neodymium Ion Dopant Effects on the Phase Transformation in Sol–Gel Derived Titania Nanostructures. *Materials Science and Engineering: B* **2004**, *111*, 150–155.
(23) Chen, H.; Nanayakkara, C. E.; Grassian, V. H. Titanium Dioxide Photocatalysis in Atmospheric Chemistry. *Chemical reviews* **2012**, *112*, 5919–5948.
(24) Jo, W.-K.; Kim, J.-T. Application of Visible-Light Photocatalysis with Nitrogen-Doped or Unmodified Titanium Dioxide for Control of Indoor-Level Volatile Organic Compounds. *Journal of hazardous materials* **2009**, *164*, 360–366.
(25) Han, Z.; Chang, V.-W.; Wang, X.; Lim, T.-T.; Hildemann, L. Experimental Study on Visible-Light Induced Photocatalytic Oxidation of Gaseous Formaldehyde by Polyester Fiber Supported Photocatalysts. *Chemical engineering journal* **2013**, *218*, 9–18.
(26) Hussain, M.; Russo, N.; Saracco, G. Photocatalytic Abatement of VOCs by Novel Optimized TiO2 Nanoparticles. *Chemical Engineering Journal* **2011**, *166*, 138–149.
(27) Rengifo-Herrera, J. A.; Osorio-Vargas, P.; Pulgarin, C. A Critical Review on N-Modified TiO2 Limits to Treat Chemical and Biological Contaminants in Water. Evidence That Enhanced Visible Light Absorption Does Not Lead to Higher Degradation Rates under Whole Solar Light. *Journal of Hazardous Materials* **2022**, *425*, 127979
(28) Vélez-Peña, E.; Pérez-Obando, J.; Pais-Ospina, D.; Marín-Silva, D. A.; Pinotti, A.; Cánneva, A.; Donadelli, J. A.; Damonte, L.; Pizzio, L. R.; Osorio-Vargas, P.; Rengifo-Herrera, J. A. Self-Cleaning and Antimicrobial Photo-Induced Properties under Indoor Lighting Irradiation of Chitosan Films Containing Melon/TiO2 Composites. *Applied Surface Science* **2020**, *508*, 144895.

(29) Le Béchec, M.; Kinadjian, N.; Ollis, D.; Backov, R.; Lacombe, S. Comparison of Kinetics of Acetone, Heptane and Toluene Photocatalytic Mineralization over TiO2 Microfibers and Quartzel® Mats. *Applied Catalysis B: Environmental* **2015**, *179*, 78–87.
(30) Hussain, M.; Ceccarelli, R.; Marchisio, D. L.; Fino, D.; Russo, N.; Geobaldo, F. Synthesis, Characterization, and Photocatalytic Application of Novel TiO2 Nanoparticles. *Chemical Engineering Journal* **2010**, *157*, 45–51.
(31) Di Paola, A.; Bellardita, M.; Palmisano, L. Brookite, the Least Known TiO2 Photocatalyst. *Catalysts* **2013**, *3*, 36–73.
(32) Pfeifer, V.; Erhart, P.; Li, S.; Rachut, K.; Morasch, J.; Brötz, J.; Reckers, P.; Mayer, T.; Rühle, S.; Zaban, A. Energy Band Alignment between Anatase and Rutile TiO2. *The Journal of Physical Chemistry Letters* **2013**, *4*, 4182–4187.
(33) Wang, C.; Wu, T. TiO2 Nanoparticles with Efficient Photocatalytic Activity towards Gaseous Benzene Degradation. *Ceramics International* **2015**, *41*, 2836–2839.
(34) Guimaraes, R. R.; Parussulo, A. L.; Araki, K. Impact of Nanoparticles Preparation Method on the Synergic Effect in Anatase/Rutile Mixtures. *Electrochimica Acta* **2016**, *222*, 1378–1386.
(35) Bianchi, C. L.; Gatto, S.; Pirola, C.; Naldoni, A.; Di Michele, A.; Cerrato, G.; Crocellà, V.; Capucci, V. Photocatalytic Degradation of Acetone, Acetaldehyde and Toluene in Gas-Phase: Comparison between Nano and Micro-Sized TiO2. *Applied Catalysis B: Environmental* **2014**, *146*, 123–130.
(36) Verbruggen, S. W. TiO2 Photocatalysis for the Degradation of Pollutants in Gas Phase: From Morphological Design to Plasmonic Enhancement. *Journal of Photochemistry and Photobiology C: Photochemistry Reviews* **2015**, *24*, 64–82.
(37) Nakata, K.; Fujishima, A. TiO2 Photocatalysis: Design and Applications. *Journal of photochemistry and photobiology C: Photochemistry Reviews* **2012**, *13*, 169–189.
(38) Kosten, E. D.; Kayes, B. M.; Atwater, H. A. Experimental Demonstration of Enhanced Photon Recycling in Angle-Restricted GaAs Solar Cells. *Energy & Environmental Science* **2014**, *7*, 1907–1912.
(39) Yu, Z.; Raman, A.; Fan, S. Thermodynamic Upper Bound on Broadband Light Coupling with Photonic Structures. *Physical review letters* **2012**, *109*, 173901.
(40) Yao, Y.; Yao, J.; Narasimhan, V. K.; Ruan, Z.; Xie, C.; Fan, S.; Cui, Y. Broadband Light Management Using Low-Q Whispering Gallery Modes in Spherical Nanoshells. *Nature communications* **2012**, *3*, 1–7.
(41) Tsai, M.-L.; Tu, W.-C.; Tang, L.; Wei, T.-C.; Wei, W.-R.; Lau, S. P.; Chen, L.-J.; He, J.-H. Efficiency Enhancement of Silicon Heterojunction Solar Cells via Photon Management Using Graphene Quantum Dot as Downconverters. *Nano letters* **2016**, *16*, 309–313.
(42) Tsai, Y.-L.; Lai, K.-Y.; Lee, M.-J.; Liao, Y.-K.; Ooi, B. S.; Kuo, H.-C.; He, J.-H. Photon Management of GaN-Based Optoelectronic Devices via Nanoscaled Phenomena. *Progress in Quantum Electronics* **2016**, *49*, 1–25.
(43) Cho, C.; Jeong, S.; Choi, H.-J.; Shin, N.; Kim, B.; Jeon, E.; Lee, J.-Y. Toward Perfect Light Trapping in Thin-film Photovoltaic Cells: Full Utilization of the Dual Characteristics of Light. *Advanced Optical Materials* **2015**, *3*, 1697–1702.
(44) Lee, W.; Jeong, S.; Lee, C.; Han, G.; Cho, C.; Lee, J.-Y.; Kim, B. J. Self-Organization of Polymer Additive, Poly (2-vinylpyridine) via One-Step Solution Processing to Enhance the Efficiency and Stability of Polymer Solar Cells. *Advanced Energy Materials* **2017**, *7*, 1602812.
(45) Wang, Y.; Li, T.; Yao, Y.; Li, X.; Bai, X.; Yin, C.; Williams, N.; Kang, S.; Cui, L.; Hu, L. Dramatic Enhancement of CO2 Photoreduction by Biodegradable Light-Management Paper. *Advanced Energy Materials* **2018**, *8*, 1703136.
(46) Bernadet, S.; Tavernier, E.; Ta, D.-M.; Vallée, R. A.; Ravaine, S.; Fecant, A.; Backov, R. Bulk Photodriven CO2 Conversion through TiO2@ Si (HIPE) Monolithic Macrocellular Foams. *Advanced Functional Materials* **2019**, *29*, 1807767.
(47) Garcia, N.; Genack, A. Z.; Lisyansky, A. A. Measurement of the Transport Mean Free Path of Diffusing Photons. *Physical Review B* **1992**, *46*, 14475.
(48) Carn, F.; Colin, A.; Achard, M.-F.; Deleuze, H.; Sellier, E.; Birot, M.; Backov, R. Inorganic Monoliths Hierarchically Textured via Concentrated Direct Emulsion and Micellar Templates. *Journal of Materials Chemistry* **2004**, *14*, 1370–1376.

(49) Silverstein, M. S. Emulsion-Templated Polymers: Contemporary Contemplations. *Polymer* **2017**, *126*, 261–282.
(50) Brun, N.; Ungureanu, S.; Deleuze, H.; Backov, R. Hybrid Foams, Colloids and beyond: From Design to Applications. *Chemical Society Reviews* **2011**, *40*, 771–788.
(51) Roucher, A.; Depardieu, M.; Pekin, D.; Morvan, M.; Backov, R. Inorganic, Hybridized and Living Macrocellular Foams:"Out of the Box" Heterogeneous Catalysis. *The Chemical Record* **2018**, *18*, 776–787.
(52) Gaikwad, P.; Ungureanu, S.; Backov, R.; Vynck, K.; Vallée, R. A. Photon Transport in Cylindrically-Shaped Disordered Meso-Macroporous Materials. *Optics express* **2014**, *22*, 7503–7513.
(53) Bachelard, N.; Gaikwad, P.; Backov, R.; Sebbah, P.; Vallée, R. A. Disorder as a Playground for the Coexistence of Optical Nonlinear Effects: Competition between Random Lasing and Stimulated Raman Scattering in Complex Porous Materials. *ACS photonics* **2014**, *1*, 1206–1211.
(54) Gaikwad, P.; Bachelard, N.; Sebbah, P.; Backov, R.; Vallée, R. A. Competition and Coexistence of Raman and Random Lasing in Silica-/Titania-Based Solid Foams. *Advanced Optical Materials* **2015**, *3*, 1640–1651.
(55) Pickering, S. U. Cxcvi.—Emulsions. *Journal of the Chemical Society, Transactions* **1907**, *91*, 2001–2021.
(56) Binks, B. P. Particles as Surfactants—Similarities and Differences. *Current opinion in colloid & interface science* **2002**, *7*, 21–41.
(57) Leal-Calderon, F.; Schmitt, V. Solid-Stabilized Emulsions. *Current Opinion in Colloid & Interface Science* **2008**, *13*, 217–227.
(58) Destribats, M.; Faure, B.; Birot, M.; Babot, O.; Schmitt, V.; Backov, R. Tailored Silica Macrocellular Foams: Combining Limited Coalescence-based Pickering Emulsion and Sol–Gel Process. *Advanced Functional Materials* **2012**, *22*, 2642–2654.
(59) Glatter, O. Data Treatment. In *Small angle X-ray scattering*; 1982.
(60) Sosnov, E. A.; Malkov, A. A.; Malygin, A. A. Hydrolytic Stability of the Si–O–Ti Bonds in the Chemical Assembly of Titania Nanostructures on Silica Surfaces. *Russian Chemical Reviews* **2010**, *79*, 907.
(61) Zhu, Z.; Wu, S.; Long, Y.; Zhang, L.; Xue, X.; Yin, Y.; Xu, B. Phase-Transition Kinetics of Silicon-Doped Titanium Dioxide Based on High-Temperature X-Ray-Diffraction Measurements. *Journal of Solid State Chemistry* **2021**, *303*, 122544.
(62) Bolis, V.; Busco, C.; Ciarletta, M.; Distasi, C.; Erriquez, J.; Fenoglio, I.; Livraghi, S.; Morel, S. Hydrophilic/Hydrophobic Features of TiO2 Nanoparticles as a Function of Crystal Phase, Surface Area and Coating, in Relation to Their Potential Toxicity in Peripheral Nervous System. *Journal of colloid and interface science* **2012**, *369*, 28–39.
(63) Zhu, J. X.; Pine, D. J.; Weitz, D. A. Internal Reflection of Diffusive Light in Random Media. *Physical Review A* **1991**, *44*, 3948.
(64) Vincent, G.; Marquaire, P.-M.; Zahraa, O. Abatement of Volatile Organic Compounds Using an Annular Photocatalytic Reactor: Study of Gaseous Acetone. *Journal of Photochemistry and Photobiology A: Chemistry* **2008**, *197*, 177–189.
(65) Peral, J.; Ollis, D. F. Heterogeneous Photocatalytic Oxidation of Gas-Phase Organics for Air Purification: Acetone, 1-Butanol, Butyraldehyde, Formaldehyde, and m-Xylene Oxidation. *Journal of Catalysis* **1992**, *136*, 554–565.
(66) Sauer, M. L.; Ollis, D. F. Acetone Oxidation in a Photocatalytic Monolith Reactor. *Journal of catalysis* **1994**, *149*, 81–91.
(67) Bettoni, M.; Candori, P.; Falcinelli, S.; Marmottini, F.; Meniconi, S.; Rol, C.; Sebastiani, G. V. Gas Phase Photocatalytic Efficiency of TiO2 Powders Evaluated by Acetone Photodegradation. *Journal of Photochemistry and Photobiology A: Chemistry* **2013**, *268*, 1–6.
(68) Vorontsov, A. V.; Kurkin, E. N.; Savinov, E. N. Study of TiO2 Deactivation during Gaseous Acetone Photocatalytic Oxidation. *Journal of catalysis* **1999**, *186*, 318–324.
(69) Qi, J.; Li, J.; Li, Y.; Fang, X.; Sun, X.; Shen, J.; Han, W.; Wang, L. Synthesis of Porous Carbon Beads with Controllable Pore Structure for Volatile Organic Compounds Removal. *Chemical Engineering Journal* **2017**, *307*, 989–998.

(70) Zeng, W.; Bai, H. Adsorption/Desorption Behaviors of Acetone over Micro-/Mesoporous SBA-16 Silicas Prepared from Rice Husk Agricultural Waste. *Aerosol and Air Quality Research* **2016**, *16*, 2267–2277.
(71) Drisko, G. L.; Zelcer, A.; Wang, X.; Caruso, R. A.; Soler-Illia, G. J. de A. Synthesis and Photocatalytic Activity of Titania Monoliths Prepared with Controlled Macro-and Mesopore Structure. *ACS applied materials & interfaces* **2012**, *4*, 4123–4130.
(72) Thejaswini, T. V.; Prabhakaran, D. Synthesis of Mesoporous Titania–Silica Monolith Composites—a Comprehensive Study on Their Photocatalytic Degradation of Acid Blue 113 Dye under UV Light. *International Journal of Nanoscience* **2016**, *15*, 1660012.

TOC